CFD Investigation of Wind Turbine Rotor Design Parameters

S. Gómez-Iradi and G.N. Barakos

CFD Laboratory, The University of Liverpool Liverpool, L6 97ZF, United Kingdom http://www.liv.ac.uk/engdept

Abstract

This article presents an investigation of the relative importance of key design parameters of a HAWT blade. CFD is used as the main tool, after validation against experimental data of the NREL/NASA-Ames Phase VI wind tunnel campaign. Tip and root sections, blade aspect ratio and pitch angle are analysed and all CFD calculations were performed using a compressible Reynolds-averaged Navier-Stokes solver. The selected case corresponds to 7 m/s upwind wind turbine at 0° of yaw angle and a rotational speed of 72 rpm. Various root and tip configurations were considered and the obtained results indicate that the exact representation of the root and tip geometry of a HAWT has an small but finite effect in the thrust and torque levels at working conditions. This effect is however secondary to the effects of aspect ratio and blade pitch.

1 Introduction

In order to maximise power output at minimum cost, a trend is been established to increase the aspect ratio of wind turbine blades. This objective comes with the requirement to improve the aerodynamic performance of wind turbines blades and optimise their aerodynamics at design conditions. Betz's theory marks the maximum output of a wind turbine aerodynamic extraction and modern wind turbine designs reach the 48% as maximum and 25% when nominal power output is reached [1]. In addition, as the size of wind turbines increases manufacturers go away from their knowledge base (the largest blade in production is 61.5 m long) and there are no working examples to use as prototypes or starting points for design. Prediction of HAWT performance based on CFD is therefore of significant practical interest.

Regarding the prediction of the aerodynamic performance of wind turbines, CFD is a valid option for two reasons; i) cost and ii) difficulties in applying scaling laws to wind-tunnel data. These issues are related to the difficulties in achieving, in a wind tunnel during the same experiment, the same Reynolds and Mach numbers, and operational parameters of a full size wind turbine. Regardless of the success of CFD in several areas, CFD solvers still need validation against experimental data or field data. Since most Blade Element Momentum (BEM) analyses have difficulties to quantify the aerodynamic effect of the tip and root sections of the blade, due to the complex 3D nature of the flow, tip and root effect are the focus of this paper. Wind tunnel data will be used for validation so that confidence on the obtained results can be established. The comprehensive paper of Vermeer [2] presents in systematic way all experiments related to wind turbines measurements. Based on Vermeer's work, the NASA-Ames NREL Phase VI was selected due to its popularity, availability of surface pressure measurements at a survey, range of conditions, and lack of scaling, since a small-size wind turbine was used. This dataset has been the subject of many works in the international community and was made available to many researches. Finally, the experimental campaign was carried with CFD validation in mind.

Wind turbine CFD is primary carried out using incompressible solvers, due to the flow speeds encountered near the tips of the blades. The incompressible solver used in the majority of published papers related to the wind turbines is EllipSys3D [3], developed at Risø National Laboratory and Danmarks Tekniske Universitet (DTU). Other incompressible solvers including CFX [4, 5] from AEA Technologies, AVL SWIFT [6] from AVL and CFD-ACE [7] developed by Yang and Chang were also used for wind turbine computations. Furthermore, solvers designed for helicopter CFD or general-purpose were also employed for the analysis of HAWT. These are compressible solvers, for much faster flows. Overflow-D2 [8] is one of them, which was developed by NASA and is used for rotorcraft research in the USA. Other compressible CFD solvers used for wind turbines are elsA [9] developed by ONERA and CERFACS, Euranus [10] from VUB and FOI, and Flower [11] from DLR. As the trend towards higher blade tip speeds continues for the growing offshore installations, compressible flow effects must be accounted for. Morris [12], also mentions compressibility as a key asset of a solver, if aero-acoustics is to be considered. The CFD mesh sizes employed in the literature range from 1 to 12 million cells for the cases mentioned above. Multi-blocks structured grids were mainly used. There is also one exceptional case where LES was carried out on a grid of 300 million cells [13] for the analysis of a small wind turbine.

Despite most of the calculations performed with the above mentioned solvers concern isolated rotor cases [11, 14, 15], some researchers have also considered the effect of the tower [16, 17] and studied the interactions between the tower and blades as well as its effect on the turbine performance. Other works focused on the effect of the wind tunnel walls [14], while others have analysed the tip flow region [13, 18] in terms of vortex generation or aero-acoustics and the root section influence [9].

Although interactional aerodynamics, between blade and tower, ground or other turbines is important and influences the performance of wind turbines, for new designs the aerodynamics of an isolated blade must first be considered at working conditions. This is presently done using BEM and wind tunnel data. However, simple methods (BEM) have difficulties to account for root and tip effects and for this reason CFD based on a compressible flow solver will be employed in this paper to quantify the effect of the root and the tip on the overall aerodynamics of a wind turbine at design conditions. Several different HAWT configurations are to be analysed to account for tip and root section influences. For the selected cases the root part of the blade is either included or not in the CFD while flat, rounded and extended tips have been considered. The obtained CFD results are compared with the experiments from NASA-Ames Phase VI [19].

2 CFD method and grid generation

A compressible CFD method capable of solving the URANS compressible flow equations on multi-block structured grids using a cell-centred finite-volume method for spatial discretisation was employed in this work. The work on the WMB (Wind Multi-Block) CFD solver, which is suitable for the analysis of wind turbine blades is fuelled by the established trend towards large-diameter off-shore wind turbines operating at high tip speeds. This results in relatively high tip Mach numbers (of the order of 0.3 at sea-level conditions and even higher in the suction side [12]) and consequently compressibility effects can not be neglected. Although several alternatives to compressible flow solvers are available, compressible solvers offer more flexibility for the CFD developers and practitioners and can operate at a wide range of conditions. The present solver is designed to account for the relative motion of the blades, structural deformation and turbulent flow. An implicit method [20] is employed, and the resulting linear system of equations is solved using a pre-conditioned Generalised Conjugate Gradient method. For unsteady simulations, implicit dual-time stepping is used, which is based on Jameson's pseudo-time integration approach [21]. From the beginning, the solver was designed with parallel execution in mind and for this reason a divide-and-conquer approach was used to allow for multi-block grids to be computed on distributed-memory machines and especially low-cost Beowulf clusters of personal computers. Variants of this method for many aerospace applications have been detailed in references [22, 23], amongst others.

Multi-block grids have several advantages over single-block ones. One of the advantages is the flexibility in representing geometry, which allows the assessment of very complicated wind turbine configurations (see Figure 1a). A second advantage is that they can be optimised for parallel computing by minimising communication between the processors and balancing their work load. The grids for the present work were generated with the ICEM-Hexa grid generation software. The multi-block topologies employed for this work, start from a C-topology around the blade in order to resolve the suction-peak on each aerofoil section and capture its wake. In addition, the current topology allows for variations of the pitch angles without reducing the quality near the blades for the same grid. The near-blade blocks can be seen in Figure 1b and these can be kept undeformed during pitch changes. This technique is detailed in [20] reference. The current blocking uses extruded blocks from the blade tip towards the far-field boundary in a true multi-block fashion. The same topology is used from the blade root to the spinner for cases where a root section is not present.

The multi-block topologies described above were used for generating several grids, as shown in Table 1. The grids were further subdivided in blocks, in order to facilitate load balancing during parallel computations. The load balance for 24 and 48 processors is shown, for all computed cases, in Table 1.

In order to asses the sensitivity of the solution on the location of far-field boundaries, two different far-field geometries were constructed. Figures 1c and 1d highlights the differences between them and their grid characteristics are summarised in Table 1 (Cases 2Ia & 2Ib). The baseline geometry has a cylindrical shape with 8 radii of the blade as diameter in the rotor plane, 4 radii of the blade towards the inflow and another 8 towards the outflow. The modified far-field geometry is also cylindrical and has 16 blade radii as diameter in the rotor plane, 8 radii towards inflow and 16 radii towards the outflow boundary (see Figures 1c & 1d). For calculations, all grids were normalised using the maximum chord of the blade as the characteristic length. For this case was 0.737 m (1 blade radius = 6.824 chords).

3 Results and discussion

3.1 Validation data and test cases

The experiments carried out in the NASA-Ames wind tunnel Phase VI [19] are extensively used in the literature [5, 14, 24] for the reasons mentioned in the introduction. The main measured quantity is the pressure distribution along the blade chord at five span-wise sections, with 22 pressure taps placed in each section. The data set number S0700000 corresponds to 7m/s free stream wind and 72 rpm rotational speed and is used in this paper to present a working condition of the wind turbine. The geometric characteristics of the two bladed upwind rotor include 3° pitch at the tip, 0° of cone angle and 0° of yaw angle. The S809 aerofoil section was used from 25% of the span to the tip. Unfortunately, there are not any wake measurements, which could further enhance the value of this experiment and the fidelity of the CFD validation.

The definition of the geometry for the Phase VI experiments provides the blade twist and the coordinates of the S809 aerofoil section, however, the tip and root sections are not defined in an unique way. For this reason, four different attempts were made in order to quantify the relevance of these sections on the overall performance. The planform of these geometries is shown in Figures 2a to 2d and the details of the root and tip sections in Figures 3a to 3d.

Figure 2a presents an isolated blade, where no root section was taken into account, starting the blade at 25% of radius distance with the flat inboard and outboard ends. A long cylinder running between the inflow to the outflow boundaries is used to model the root attachment to the spinner. The blade tip is 5.4% longer than the experimental one. This was done so that influence of the tip at outboard stations characteristics can be quantified as given by Hand's Technical Report [19]. The difference between the configurations of Figures 2b and 2a is in the spinner. A streamlined spinner was introduced to avoid massive flow separation and for comparison with the tube configuration of Figure 2a. Figure 2c is closer to the experiments, since it has the correct aspect ratio of the blade, however, a flat tip, is used. This was done to analyse the differences between round and flat tip-caps due to the different pressure distribution they induce near the tip. The root section is also closer to the experimental since a blended section is added (see Figure 3b). The planform for Case 4 is shown in Figure 2d. This case is identical to Case 3 apart from the shape of the tip. The tip is now rounded using the camber line at the 98% of the span of the blade. The details of the sections are shown in Figures 3c and 3d. The four configurations discussed in the previous paragraphs are detailed in Table 1.

3.2 CFD Results

The case S0700000 from the NREL database was selected for this study. This case was also been studied by other authors [3, 5, 14, 15, 17, 24–28] but studies of influence of the root and tip sections are brief. Test cases at higher wind speeds have been analysed by many authors [14, 24] but since these appear to have stalled flow regions they were not considered for the analysis in this paper. At the selected wind speed of the wind the blades are loaded with 575 N each on average. To date, there is just one tip shape investigation, related to aerodynamics, published [18] and another one mentioning root section [9]. As a first step, grid convergence was investigated. For this purpose the grids 2I, 2II and 2III of Table 1 were used. The CFD results, shown in Figures 4a and 4b, indicate little differences between the fine and medium grids. However, differences do exist between the coarse and medium grids near the suction peak and the suction side of the section. The coarseness of the grid is evident even on the pressure side of the blade. A mismatch there is usually an indication of a poorly resolved flow resulting in incorrect flow angle. Based on these results, the medium grid can be used for computing this test case without significant deterioration of the obtained results, as far as the pressure field is concerned.

Once the grid density was established, the effect of the time step used for unsteady computations was investigated. The solution on grid 2III was computed using steps of 1 degree in azimuth while solutions on the 2I and 2II grids were obtained using steps of 0.25 degrees. The results shown in Figures 4a and 4b indicate that 0.25 degree steps are adequate for resolving this flow case.

Finally, the effect of the far-field location was investigated. Two grids were used as discussed in the previous section (see Figures 1c and 1d). The three components of the velocity vector obtained on the two grids are plotted in Figure 5a to 5c. The contours are taken at half radii downwind of the wind turbine (see schematic in Figure 5d). The flow area near the blade is not significantly affected by the location of the far-field boundary. Since this work focuses on the blade area, the boundaries of the grid 2Ia were selected for subsequent computations.

For comparison against experiments, the CFD data had to be probed at the location of the pressure taps. Then, the highest value of pressure had to be found and used as the reference for computing the surface pressure coefficient exactly as reported in [19]. For the calculation of integrated loads, readings from 22 pressure taps, located exactly like the experiment, where extracted from the CFD and integrated. This was needed in order to have the same accuracy of integration, as for the experiments, in the comparisons.

3.2.1 Root section

The effect of the root section was then quantified using Cases 1, 2 and 3. Cases 1 and 2 have no root section though Case 3 has. Furthermore, Cases 2 and 3 have a spinner while Case 1 has an infinite tube as inner boundary. The planform of these cases is shown in Figures 2a, 2b and 2c, and the detailed view of the root sections in Figures 3a and 3b.

The root section added to the isolated rotor (Case 3) improves the results as expected. This can be seen analysing the pressure coefficients (C_P) at 30% station of the blade, which is shown in Figure 6b. The results for the pressure side indicated that a different incidence angle is experienced for Cases 2 and 3 due to the difference of the root vortex configurations. Case 3 shows the best comparison against experiments. The suction peak was also well captured for Case 3, while this was not the case for Cases 1 and 2. Despite this, an over-prediction of suction is observed for Case 3, which can be due to the geometrical differences with the experimental blade root section. The exact shape of this section is not precisely known. As expected, the differences are more pronounced at the inboard stations. Figure 6a presents a comparison at 27% R. There are no significant differences between Cases 1 and 2 (infinite tube and spinner) as shown in previous two figures. The stations at 46.6% and 63.3% are shown in Figures 6c and 6d and no differences are observed between the three C_P predictions for the three configurations, indicating that the effect of the root section dismissed as inboard stations are approached.

Normal and tangential coefficients (C_N & C_T) are shown in Table 2 for Cases 1 to 3 and these are compared with the experimental values. The maximum and minimum values of the experimental C_N and C_T corresponds to the experimental values at 0° azimuthal angle over 35 cycles. At 30% R the suction over-prediction of the Case 3 resulted in higher C_N than the experiment, however, at outboard stations (46.6% and 63.3%) results for Case 3 are closer to the experimental values than the other two cases.

The thrust and torque of the wind turbine blade were also calculated and they are shown in Figures 8a to 8d. Figures 8a and 8b represent thrust and torque variations for a full revolution. On the other hand, Figures 8c and 8d represent the averaged thrust and torque for CFD and experiments (azimuthal angles between 150° and 210° were excluded for the averaging because an isolated rotor was considered in the CFD computations). Thrust and torque are over-predicted for Cases 1 and 2. This is due to their higher aspect ratio blades used for the computations. Although there are differences for the C_P at 27% R and 30% R, due to the low rotational speed, this has a small effect on the overall loading of the blade.

Flow visualisation of the root region, using iso-surfaces of turbulent Reynolds number (Re_T) and coloured with pressure level are shown in Figures 9a and 9b for Cases 2 and 3, respectively. These cases show a different behaviour due to the presence of root attachement section (Figure 9b). For this configuration, shedding of vorticity is present near the root but there is no discrete vortex formed. Further outboard where an abrupt change of the blade geometry takes place, a smaller vortex is formed.

3.2.2 Tip section

Comparisons between three different blade tips were then considered. Cases 2, 3 and 4 were analysed for that purpose. Cases 2 and 3 have a flat tip while Case 4 has a rounded tip constructed by revolving the camberline at the 98% R station of the blade. On the other hand, the blades for Cases 3 and 4 have the same aspect ratio as experimental blades while Case 2 was 5.4% longer in radius. The configuration of Case 4 is the closest to the geometry used for the set of the experiments.

The aspect ratio variation has found to have significant influence towards the tip of the blade. This is shown at stations from 90% R to 98% R of the blade (Figures 7a to 7d). As can be seen, there are differences between Cases 2 and 3 concentrated

on the suction side. The higher aspect ratio blade of Case 2 has a reduced downwash and this results in differences in flow incidence. The C_N values given in Table 3 show more than 20% differences in C_N between configurations 2 and 3 and 40% in C_T. As consequence, there are also differences in the thrust and torque shown in Figures 8a and 8b. These differences highlight the lesser influence of the root section in turbine thrust and torque despite the addition of the root section adds unsteadiness into the flow.

There are also some differences between Case 3 (flat tip) and Case 4 (rounded tip). The C_P comparisons shown in Figures 7a to 7d indicate that the outer stations are influenced by this small change of blade shape. The tip vortex develops in a different way for flat and for rounded tips, and its influence slightly reaches the 90% R and 92% R stations. At 95% R (Figure 7c) this difference is significant. Despite Cases 3 and 4 being quite close to the experimental configuration, the C_P is not perfectly captured. This is probably due to the under-prediction of suction peak at outboard stations. Again, as mentioned before and as was the case with the root section, the tip geometry is not fully defined in the literature. The tangential and normal coefficients from the Table 3 highlight these differences at 95% R station. The inboards stations are almost identical between Cases 3 and 4. The thrust for each blade from Figure 8a is in agreement with the experimental results, with differences in the range of 1.5-2% with Case 3 and 1 % with Case 4 (although the thrust prediction for Case 4 is within the maximum variations of experiments as can be seen in Figure 8c). The torque, in general, is under-predicted for these cases and can be due to the few points used for the calculation. The flow visualisation around the tip sections is shown in Figures 9c to 9d. These two figures correspond to Cases 2 and 3. The tip vortex as visualised with iso-surfaces of turbulence Reynolds number (Re_T) looks similar but has larger expansion for Case 2. This is due to the slightly higher tip speed for this case. The tip vortex generated with configuration 4 is different as show the Figure 9d and is formed further towards the trailing edge of the founded tip.

3.2.3 Blade pitch angle

In order to determine the sensitivity of the obtained loads on the blade pitch angle, comparisons between two different blades were considered. Case 4 was used as a baseline configuration, which had 3° of pitch angle at the tip. A modified version was then produced which had 3.5° of pitch and the flow was computed again at 7 m/s. The change in twist has an effect though out the flow since it decreases the local incidence. Thrust was found to be 5.5% lower than the original Case 4 as can be seen in Figure 8a. On the other hand, despite that the torque was also under-predicted, its value is not far from the Case 4, being 1.4% higher than Case 4's. This is a strong visible effect and highlight the importance of correct twist values when CFD computations are considered.

4   Conclusion

Various root and tip variations of the NREL Phase VI S0700000 case were computed to quantify the relative importance of the exact geometry of these on the aerodynamic performance of a wind turbine blade. The largest differences were found in the root section, where the variation of the normal coefficient and tangential coefficients could be bigger than 10% if root section is added or the spinner is used instead of infinite tube like boundary. Despite these differences, the overall agreement with the experiments is much more influenced by the blade radius. And in this case the variation of the loads affects directly the variation in the overall agreements. To conclude, for preliminary design of wind turbine blades, first calculations can be preformed with approximate root and tip shapes while the twist distribution and aspect ratio must be precisely specified.

References

[1] A.S. Ahmed Shata and R. Hanitsch, Electricity Generation and Wind Potential Assessment at Hurghada, Egypt, *Renew Energy*, March 2007.

[2] Vermeer LJ Sørensen JN Crespo A, Wind Turbine Wake Aerodynamics, *Progress in Aerospace Sciences*, 39:467–510, 2003.

[3] Sørensen NN Johansen J, Aerofoil Characteristics from 3D CFD Rotor Computations, *Wind Energy*, 7(4):283–294, October-December 2004.

[4] Iaccarino G, Predictions of a Turbulent Separated Flow Using Commercial CFD Codes, *Journal of Fluids Engineering*, 123:819–828, December 2001.

[5] Chattot J Schmitz S, Application of a 'Parallelized Coupled Navier-Stokes/Vortex-Panel Solver' to the NREL VI Rotor, In 43rd *AIAA Aerospace Sciences Meeting and Exhibit*, Reno, Nevada, 10-13 January 2005. AIAA paper 2005-593.

[6] Beader D Basara B, Alajbegovic A, Simulation of Single- and Two-Phase Flows on Sliding Unstructured Meshes Using Finite Volume Method, *International Journal for Numerical Methods in Fluids*, 45(10):1137–1159, August 2004.

[7] W. Wolfe and S. Ochs, CFD Calculations of S809 Aerodynamic Characteristics, In 35th *AIAA Aerospace Sciences Meeting*, 1997, AIAA paper 97-0973.

[8] R.M. Kufeld, Wind Turbine Calculations and Validation, *NASA Center for AeroSpace Information (CASI) Ames Research Center Research and Technology 2000, NASA/TM-2001-210935*, (43–44), June 2002.

[9] A. Le Pape and J. Lecanu, 3D Navier-Stokes Computations of a Stall-Regulated Wind Turbine, *Wind Energy*, 7(4):309–324, October-December 2004.

[10] P. Eliasson, D. Wang, S. Meijer, and J. Nordstroem, Unsteady Euler Computations Through Non-Matching and Sliding-Zone Interfaces, In 36th *Aerospace Sciences Meeting and Exhibit*, Reno, Nevada, 12-15 January 1998. AIAA paper 1998-0371.

[11] P.K. Chaviaropoulos, I.G. Nikolaou, K.A. Aggelis, N.N. Sørensen, J. Johansen, M.O.L. Hansen, M. Gaunaa, T. von Hambraus, H.F. Geyr, C. Hirsch, K. Shun, S.G. Voutsinas, G. Tzabiras, Y. Perivolaris, and S.Z. Dyrmose, Viscous and Aeroelastic Effects on Wind Turbine Blades. The VISCEL Project. Part I: 3D Navier-Stokes Rotor Simulations, *Wind Energy*, 6(4):365–385, October-December 2003.

[12] P. Morris, L. Long, and K. Brentner, An Aeroacoustic Analysis of Wind Turbines, In 42nd *AIAA Aerospace Sciences Meeting and Exhibit*, Reno, Nevada, 5-8 January 2004. AIAA paper 2004-1184.

[13] C. Arakawa, O. Fleig, M. Iida, and M. Shimooka, Numerical Approach for Noise Reduction of Wind Turbine Blade Tip with Earth Simulator, *Journal of the Earth Simulator*, 2:11–33, March 2005.

[14] N.N. Sørensen, J.A. Michelsen, and S. Schreck, Navier-Stokes Predictions of the NREL Phase VI Rotor in the NASA Ames 80 ft x 120 ft Wind Tunnel, *Wind Energy*, 5(2-3):151–169, April-September 2002.

[15] A. LePape and V. Gleize, Improved Navier-Stokes Computations of a Stall-regulated Wind Turbine using Low Mach number Preconditioning, In 44th *Aerospace Sciences Meeting and Exhibit*, Reno, Nevada, 9-12 January 2006. AIAA paper 2006-1502.

[16] E. Duque, C.P. van Dam, and S.C. Hughes, Navier-Stokes Simulations of the NREL Combined Experiment Phase II Rotor, In 37th *Aerospace Sciences Meeting and Exhibit*, pages 143–153, Reno, Nevada, 11-14 January 1999. AIAA paper 1999-37.

[17] F. Zahle and J. Johansen, Wind Turbine Rotro-Tower Interaction Using an Incompressible Overset Grid Method, In *AIAA 45th Aerospace Sciences Meeting and Exhibit*, Reno, Nevada, 8-11 January 2007.

[18] M.O.L. Hansen and J. Johansen, Tip Studies Using CFD and Comparison with Tip Loss Models, *Wind Energy*, 7(4):343–356, October-December 2004.

[19] M.M. Hand, D.A. Simms, L.J. Fingersh, D.W. Jager, J.R. Cotrell, S. Schreck, and S.M. Larwood, Unsteady Aerodynamics Experiment Phase VI: Wind Tunnel Test Configurations and Available Data Campaigns, Technical Report NREL/TP-500-29955, NREL, December 2001.

[20] R. Steijl, G. Barakos, and K. Badcock, A Framework for CFD Analysis of Helicopter Rotors in Hover and Forward Flight, *International Journal for Numerical Methods in Fluids*, 51:819–847, January 2006.

[21] A. Jameson, Time Dependent Calculations Using Multigrid with Applications to Unsteady Flows Past Airfoils and Wings, In *AIAA 10th Computational Fluid Dynamics Conference*, Honolulu, HI, June 1991. Paper 91-1596.

[22] A. Spentzos, G. Barakos, K. Badcock, P. Richards, B.E. Wenert, S. Schreck, and M. Raffel, CFD Investigation of 2D and 3D Dynamic Stall, *AIAA Journal*, 43(5):1023–1033, May 2005.

[23] G. Barakos, R. Steijl, K. Badcock, and A. Brocklehurst, Development of CFD Capability for Full Helicopter Engineering Analysis, In *31st European rotorcraft Forum*, Florence, Italy, September 2005.

[24] E. Duque, M.D. Burklund, and W. Johnson, Navier-Stokes and Comprehensive Analysis Performance Predictions of the NREL Phase VI Experiment, In 22nd *ASME Wind Energy Simposium*, Reno, Nevada, January 2003. AIAA paper 2003-0355.

[25] S. Benjanirat and L. Sankar, Recent Improvement to a Combined Navier-Stokes/Full Potential Methodology for Modeling Horizontal Axis Wind Turbines, In 42nd *AIAA Aerospace Sciences Meeting and Exhibit*, Reno, Nevada, 5-8 January 2004. AIAA paper 2004-830.

[26] S. Schreck and M. Robinson, Rotational Augmentation of Horizontal Axis Wind Turbine Blade Aerodynamic Response, *Wind Energy*, 5(2-3):133–150, April-September 2002.

[27] G. Xu and L.N. Sankar, Application of a Viscous Flow Methodology to the NREL Phase VI rotor, In 40th *Aerospace Sciences Meeting and Exhibit*, Reno, Nevada, 14-17 January 2002. AIAA paper 2002-0030.

[28] D.J. Laino, A.C. Hansen, and J.E. Minnema, Validation of the AeroDyn Subroutines Using NREL Unsteady Aerodynamics Experiment Data, pages 179–189, Reno, Nevada, 14-17 January 2002. AIAA paper 2002-39.

Cases	(Number of Blocks)	(Number of Blocks)	(Number of Blocks)	processors	Radius (R)
4p	1,693,456 (250)	31,030 (76)	3,886 (11)	98.7 % / 97.2 %	I: 2, O: 4, FF: 4

4p: Blade pitch angle 0.5° higher than the rest of the Cases. I: Inflow. O: Outflow. FF: Far-field.

Table 1: Different configurations and their properties (half domains are used due to the symmetry except for the load balance, where full configuration was considered).

	Stations	30 %	46.6%	63.3%		30 %	46.6%	63.3%
Case 4p	C_N	0.846	0.987	0.923	C_T	0.089	0.114	0.092

Table 2: Blade loads for the root section at experimental blade azimuth angle of 0°.

	Stations	63.3%	80%	95%		63.3%	80%	95%
Case 4p	C_N	0.923	0.713	0.446	C_T	0.091	0.063	0.026

Table 3: Blade loads for the tip section at experimental blade azimuth angle of 0°.

(a) Blocks edges around the blade and spinner. (b) Blocks of the multi-block topology. (c) Top view of far-field boundaries. (d) Front view of far-field boundaries.
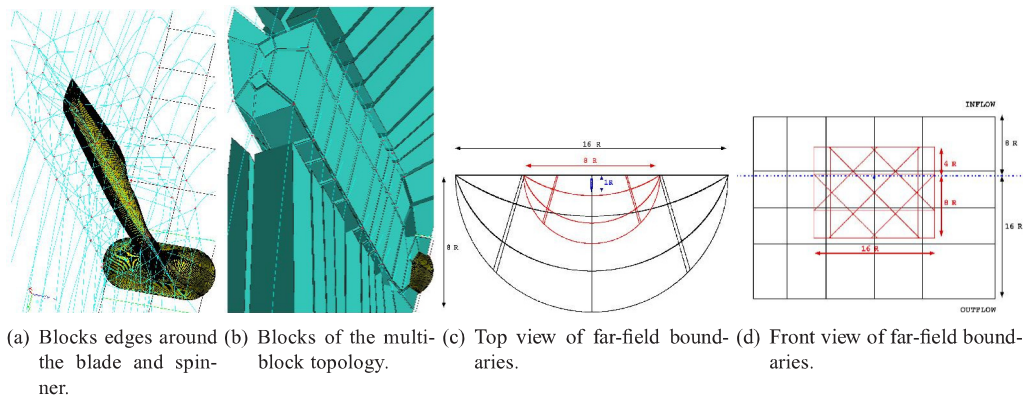
Figure 1: Multi-block topology and the far-field boundaries for the CFD analysis of HAWT. (a) The volume edges are shown. (b) The C-type blocking around the blade is shown. (c) Top view of the single and double geometry far-field. (d) Front view of the single and double geometry far-field.
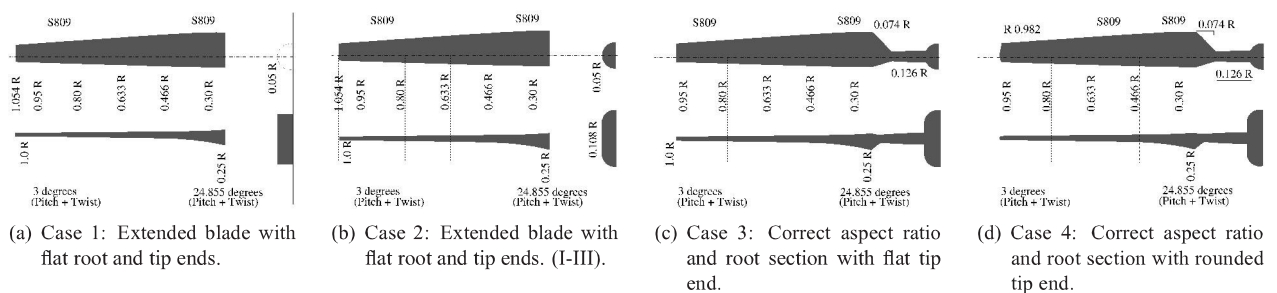

(a) Case 1: Extended blade with flat root and tip ends. (b) Case 2: Extended blade with flat root and tip ends. (I-III). (c) Case 3: Correct aspect ratio and root section with flat tip end. (d) Case 4: Correct aspect ratio and root section with rounded tip end.

Figure 2: Four different configurations used to analyse the influence of root, tip and aspect ratio influence.

(a) Spinner without root section (Cases 1 & 2).

(b) Spinner with root section (Cases 3, 4 & 4p).

(c) Flat tip (Cases 1, 2 & 3).
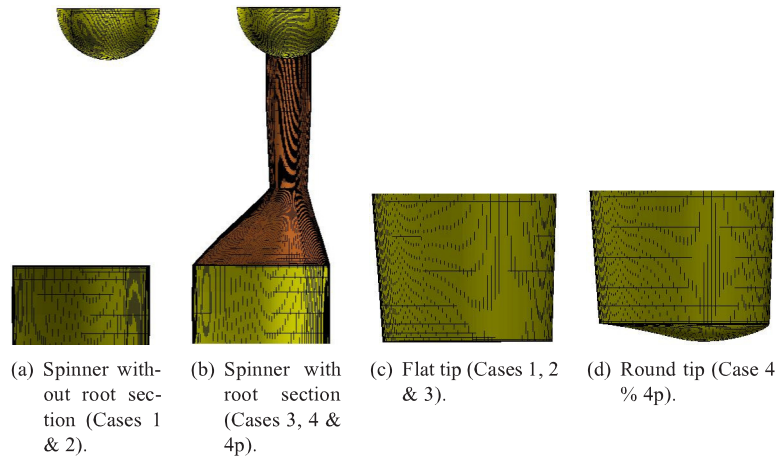
(d) Round tip (Case 4 % 4p).

Figure 3: Tip and root details for the different configurations employed in this work. Top view of the tip and root (see a,b,d & e). Side view of the blade (see c & f).
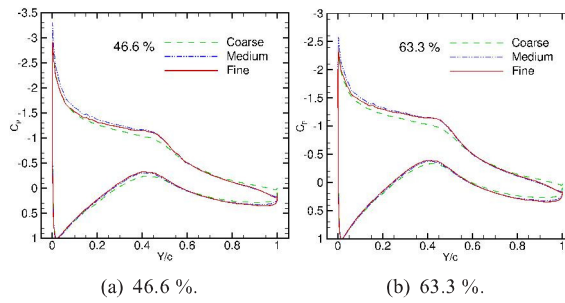

(a) 46.6 %.

(b) 63.3 %.

Figure 4: Grid size dependence for Case 2, where the rotor blades had larger aspect ratio and no root section. The half grid sizes and the azimuthal variation in degrees per time step are: Coarse (660,644 & 0.25°) dashed green, Medium (1,693,586 & 0.25°) dash-dot-dot blue and Fine (2,276,152 & 1°) solid red.

(a) U/V_∞ velocity component.

(b) V/V_∞ velocity component.

(c) W/V_∞ velocity component.
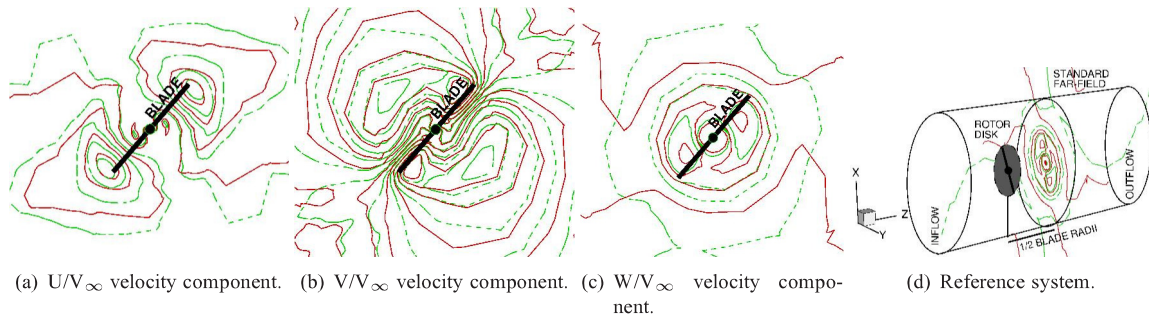
(d) Reference system.

Figure 5: Effect of far-field. Solid red line represents Case 2Ia (standard far-field) from Table 1 while 2Ib (double distance of the boundaries) is presented as dashed green lines. The two blades are represented as a thick black line and the spinner as a black circle.
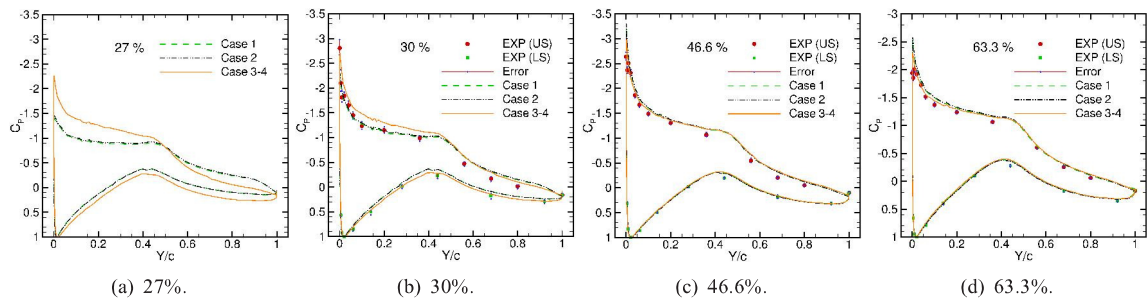

(a) 27%.

(b) 30%.

(c) 46.6%.

(d) 63.3%.

Figure 6: Blade pressure coefficients extracted at span-wise station between the root and middle radius of the blade. Comparisons are shown for four different root configurations (Cases 1-4) at experimental blade azimuth angle of 0°.

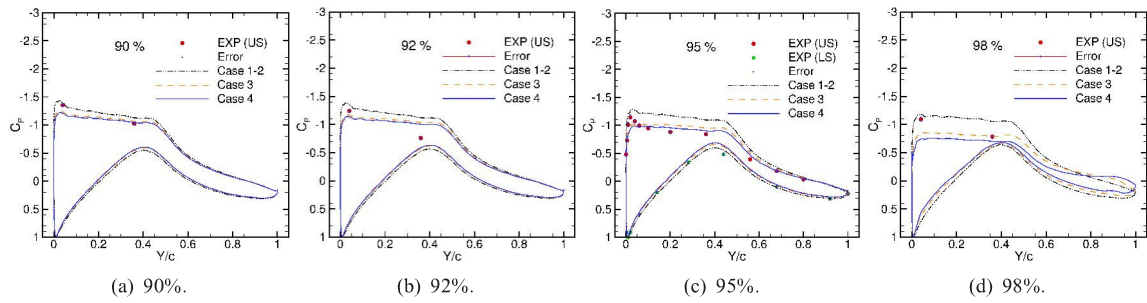(a) 90%.　　(b) 92%.　　(c) 95%.　　(d) 98%.

Figure 7: Blade pressure coefficients extracted at span-wise station near the tip of the rotor. Comparisons are shown for the flat (Cases 1-3) and rounded (Case 4) tips at experimental blade azimuth angle of 0°.

(a) Thrust.　　(b) Torque.　　(c) Averaged thrust.　　(d) Averaged torque.
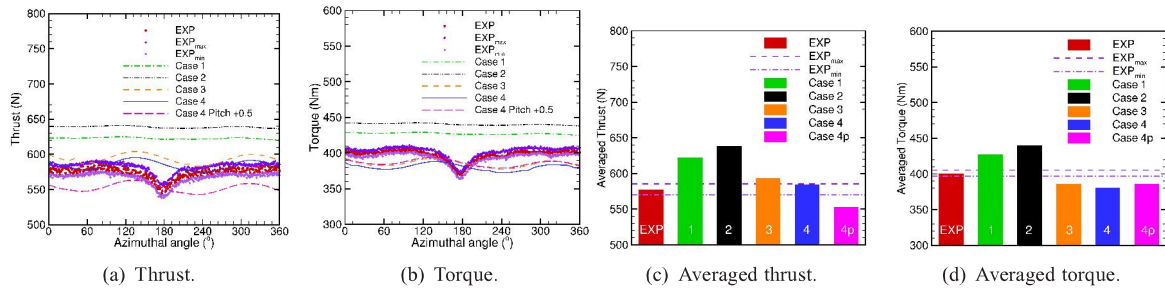
Figure 8: Single blade thrust and torque for five different cases. The CFD calculations were performed for an isolated rotor, so they did not take into account the effect of the tower that can be appreciated between 120° and 240° on the experimental data. The unsteadiness of the calculations is shown in the CFD results despite three full revolutions were computed for each Case. Figures c-d are averaged thrust and torque results from experiments and CFD computations.

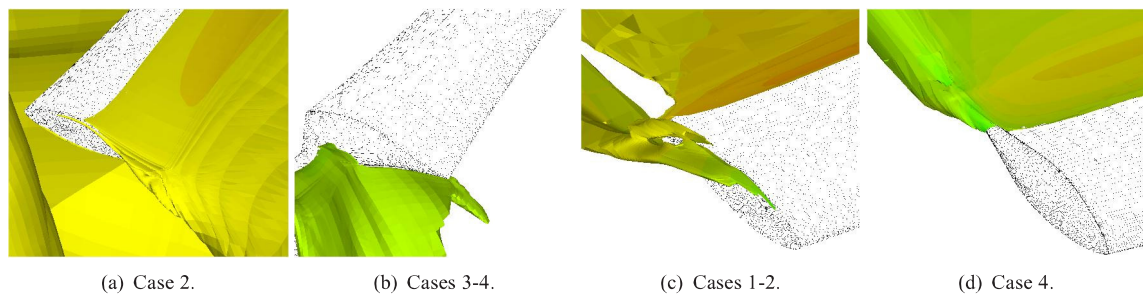(a) Case 2.　　(b) Cases 3-4.　　(c) Cases 1-2.　　(d) Case 4.

Figure 9: Flow visualisation: Reynolds Turbulent number iso-surfaces with Pressure contours around the tip for the four analysed cases.